

# A Deep-Learning Method for Path Loss Prediction Using Geospatial Information and Path Profiles

Takahiro Hayashi<sup>✉</sup> and Koichi Ichige<sup>✉</sup>, *Member, IEEE*

**Abstract**—Beyond 5G/6G should provide services everywhere, and it is necessary to expand area coverage and develop high-frequency bands from millimeter waves to terahertz waves. Based on these issues, clarifying radio propagation characteristics and modeling techniques is important for the system and area design of beyond 5G/6G, which will utilize various frequencies in any environment. We have developed a site-specific path loss model by extracting features of the propagation environment by machine learning using images of three regions as input data: the transmitting point, the receiving point, and the region between both points. However, image scaling is required in the region between the points to keep the image size constant in accordance with the distance. Therefore, even if the propagation path is the same, the effect on the propagation characteristics caused by shadowing is different. In this article, we propose a method to parameterize the environment on the propagation path in the region between the transmitting and receiving points with a constant size regardless of distance and combine it with images around the points. Since the dominant path that contributes to path loss characteristics depends on the urban structure between transmitting and receiving points, parameterizing the environment on the propagation path should improve the estimation accuracy. We demonstrate the effectiveness of the proposed method through an evaluation using 800-MHz and 2-GHz measured data in urban, suburban, and rural areas.

**Index Terms**—Beyond 5G mobile communication, convolution neural networks (NNs), deep neural network (DNN), machine learning, path loss prediction, path profile, principal component analysis.

## I. INTRODUCTION

BEYOND 5G/6G should provide services to drones, flying cars, ships, space stations, and places that conventional mobile communication networks have yet to cover. Therefore, it is necessary to expand the area coverage, develop high-frequency bands from millimeter waves to terahertz waves, and further improve the frequency utilization and power efficiencies. Based on these issues, the clarification of radio propagation characteristics and modeling techniques is

Manuscript received 26 December 2022; revised 6 June 2023; accepted 9 July 2023. Date of publication 20 July 2023; date of current version 6 September 2023. (*Corresponding author: Koichi Ichige*.)

Takahiro Hayashi is with KDDI Research, Inc., Fujimino, Saitama 356-8502, Japan, and also with the Department of Electrical and Computer Engineering, Yokohama National University, Yokohama 240-8501, Japan (e-mail: ta-hayashi@kddi.com).

Koichi Ichige is with the Department of Electrical and Computer Engineering, Yokohama National University, Yokohama 240-8501, Japan (e-mail: koichi@ynu.ac.jp).

Color versions of one or more figures in this article are available at <https://doi.org/10.1109/TAP.2023.3295890>.

Digital Object Identifier 10.1109/TAP.2023.3295890

important for the system and area design of beyond 5G/6G, which will utilize various frequencies in any environment.

The approaches for predicting radio propagation characteristics can be roughly divided into two categories: theoretical and statistical. Theoretical approaches, such as the finite-difference time-domain (FDTD) method [2] and ray tracing [3], [4], simulate the propagation environment and calculate the analytical radio propagation characteristics based on the electromagnetic field theory. In this approach, the estimation accuracy is greatly affected by how precisely the propagation environment is modeled. Although the accuracy is improved by precisely modeling structures, predicting path loss over a wide area demands enormous calculation time. Therefore, algorithms have been studied to reduce the calculation time [5]. The statistical approach models radio propagation characteristics by multiple regression analysis using environmental parameters such as average building height and road width in the surrounding area and measurement data. Examples are the Okumura–Hata [6] and Walfisch–Ikegami models [7], [8]. While this approach can be expected to improve prediction accuracy by using many parameters that affect radio propagation characteristics, the experience and knowledge of engineers are required to determine the environmental parameters and function. Since the number of experimental parameters has increased, it is difficult to derive an appropriate function when performing multiple regression analyses. In other words, the radio propagation characteristics are based on the interactions of various factors in the propagation environment, which increases the number of parameters to be considered, complicates the model equation, and makes it very difficult to design manually. Therefore, machine learning based on the automatic modeling of the relationship between input data and results necessary for the unsolved problem is expected.

Several methods for radio propagation prediction using machine learning have been proposed [9], [10], [11], [12], [13], [14], [15], [16], [17], [18], [19], [20], [21], [22], [29], [30]. In such methods, a training dataset is constructed from ray tracing and measurement data, and a prediction model is built by supervised learning. These methods can be applied to various environments as long as a dataset is available, but quantifying the parameters related to the propagation environment and using them as input is important. In [9], the distance between the transmitting and receiving points, base station antenna height, elevation angle with elevation on the line-of-sight (LOS), land use classification, and type of vegetation around the receiving point are used to parameterize

the propagation environment, and these data are used as input data to a neural network (NN). In [10], the optimal structure for applying an NN to path loss prediction is discussed. In the literature, the input data are parameterized using the path loss calculated by a standard path loss model and the crossed distance in each clutter, such as buildings and terrain. In [11], the propagation environment is parameterized using the LOS or non-line-of-sight (NLOS) between the transmitting and receiving points, diffraction points, and the number of penetrations into buildings and modeled by a deep NN (DNN). These methods have been reported to predict with higher estimation accuracy than models based on conventional statistical approaches. However, since the generation of input data requires extracting numerical parameters related to the propagation environment from a certain range, feature extraction requires a high cost. In addition, when the propagation environment parameters are quantified, they are treated as statistical values such as the average and frequency. Thus, location-specific information may be missed. In [12] and [13], satellite images are directly input to a convolutional NN (CNN), which is often used in the field of image recognition, to extract the features of the propagation environment to predict the path loss or its distribution. While satellite images contain much location-specific information, they are always suitable for directly determining the shapes of buildings and roads, which affect radio propagation characteristics. Imai et al. [14], Thrane et al. [15], Kuno et al. [16], and Sotirodus et al. [17] used building maps generated from OpenStreetMap and 3-D building data to more directly consider building information, which significantly affects radio propagation characteristics, and achieved estimation accuracy equivalent to or better than that of satellite images. However, the relationship between the type of input image data (e.g., OpenStreetMap or satellite images), the region, and the estimation accuracy in various areas has not been sufficiently discussed.

To improve the aforementioned problems, we have proposed a method that uses the type and region of image data and numerical parameters as input data [18], [19], [20]. Numerical parameters include the distance between the transmitting and receiving points, the azimuth of the receiving points from the transmitting point, and other numerical data related to the positional relationship between the points, as well as transmitting station parameters, such as transmission power, antenna gain, and antenna height. Aerial photographs, building maps, or building maps estimated from aerial photographs are used for the image data at the transmitting and receiving points and the intermediate point between them. In the machine learning model, convolution and pooling layers extract the input image data as features. These features and numerical parameters are input to the fully connected NN (FNN) to predict radio propagation. The evaluation with a dataset consisting of measurement data in central Tokyo shows that it can predict with higher accuracy than a model using only FNN. However, the input spatial data may include overlapping or missing areas due to differences in the distance between the transmitting and receiving points. To solve these problems, we proposed a method that acquires and uses a single image

of the area between the transmitting and receiving points [21], [22]. However, since the image size is scaled in accordance with the distance, even if the propagation path is identical, the effect on the propagation characteristics caused by the surrounding buildings is different, which limits the improvement in estimation accuracy.

In this article, we propose a method to improve the estimation accuracy of path loss prediction by combining the advantage of relating location-specific environment information by using image data around the transmitting and receiving points, i.e., multidimensional data, with environmental parameters related to the propagation path between transmitting and receiving points as features. The main contributions are described in the following.

- 1) The proposed method uniquely parameterizes environmental parameters related to the propagation path between transmitting and receiving points regardless of distance.
- 2) Improved path loss estimation accuracy by using image data around the transmitting and receiving points together with environmental parameters related to the propagation path between the points.
- 3) We evaluate the proposed method's effectiveness using the measurement data at 800 MHz and 2 GHz obtained over a wide area of approximately 500 km<sup>2</sup> in urban, suburban, and rural areas.
- 4) We clarify the image data type suitable for geographical features by evaluating the three areas in accordance with whether they are urban, suburban, or rural.
- 5) We clarify that the proposed method is effective regardless of the frequency band.

This article is organized as follows. Section II describes the approach for path loss prediction using an NN. Section III describes the proposed method using map data around the transmitting and receiving points together with environmental parameters related to the propagation path between the points. After explaining the dataset and evaluation method in Section IV, the results and discussions are presented in Section V. Finally, Section VI summarizes this article.

## II. NN FOR PATH LOSS PREDICTION

A model in which the slope of path loss concerning distance is constant is called a single-slope model, and the simplest such model is the floating intercept (FI) model expressed in the following equation:

$$PL(d) = \beta + 10\alpha \log_{10}(d) + X \text{ [dB]} \quad (1)$$

where  $d$  is the distance between the transmitting and receiving points,  $\alpha$  and  $\beta$  represent the slope and intercept, respectively, and  $X$  is the shadow fading (SF), which can be expressed as a zero-mean Gaussian random variable with a standard deviation. The parameters  $\alpha$  and  $\beta$  are the coefficients obtained by performing regression on the measurement data. The alpha-beta-gamma (ABG) model includes a distance and frequency term and is expressed in the following equation:

$$PL(d, f) = 10\alpha \log_{10}(d) + \beta + 10\gamma \log_{10}(f) + X \text{ [dB]} \quad (2)$$

where  $\gamma$  is the coefficient for the frequency dependence of the path loss and  $f$  is the frequency (GHz). This model has been used in standardizations such as WINNER II and 3GPP [23], [24]. In these models, the values of  $\alpha$ ,  $\beta$ , and  $\gamma$  are defined for various scenarios derived from use cases assumed for mobile communication systems. However, since the path loss characteristics are affected by differences in antenna height and the surrounding environment, the estimation accuracy obtained by regression of measurement data in a real environment is limited. Therefore, by including parameters other than the distance between transmitting and receiving points and frequency, such as antenna height and the surrounding propagation environment, the expression of the propagation model for the environment is improved [25], [26]. However, a large number of work-hours are required to construct the functional form of the propagation model and to extract and generate the parameters. Therefore, by using an NN that can learn the features needed to solve a problem from input data, it should learn the environmental parameters needed for path loss prediction from input data such as maps and other spatial information.

In this article, we construct a learning model that combines spatial information data, such as aerial photographs and building occupancy, with environmental parameters related to the propagation path between transmitting and receiving points obtained from these data. To distinguish structures that affect the magnitude of shadowing, such as buildings and vegetation, from spatial data, it is important to select and parameterize regions that consider not only the resolution of the spatial data but also the mechanism of radio propagation. The purpose of learning is to obtain a regression model that predicts path loss, which is expressed as follows:

$$z_n = f(x_n, \mathbf{w}, \theta) + \varepsilon \text{ [dB]} \quad (3)$$

where  $f$  is the function to learn,  $x_n$  is the input data,  $\mathbf{w}$  is the weighting matrix,  $\theta$  are the hyperparameters, and  $\varepsilon$  is the Gaussian distributed noise. We define the input data to the model as follows:

$$x_n = [d, A, S] \quad (4)$$

where  $d$  is the linear distance between the transmitting and receiving points,  $A$  is the aerial photograph or building occupancy image in accordance with the area, and  $S$  is an environmental parameter related to the propagation path between the transmitting and receiving points. The observation  $Z_n$  is obtained by measuring the reference signal received power (RSRP) of the LTE reference signal and calculating the path loss from the base station parameters. To learn such a function  $f$ , we construct a model in which the spatial information data  $x_n = [A]$  are used as input data, and the feature maps extracted by convolutional and pooling layers and  $x_n = [d, S]$  are input to the FNN.

#### A. Fully Connected Neural Network

A forward propagating NN [27] is an NN that has a structure in which units arranged in the layer are coupled only between adjacent layers, and information propagates only in

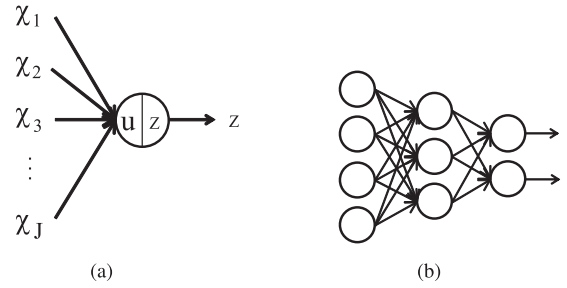


Fig. 1. Feedforward NN. (a) Units. (b) Multilayer network.

one direction from the input side to the output side. Each unit in a network receives  $J$  inputs and computes one output, as shown in Fig. 1(a). The total input  $u$  in this unit is obtained by multiplying each input  $\{x_1, x_2, \dots, x_J\}$  by different weights  $\{w_1, w_2, \dots, w_J\}$  and summing them, plus a bias  $b$ , which is defined as follows:

$$u = \sum_{j=1}^J w_j x_j + b. \quad (5)$$

The following equation expresses the output  $z$  of this unit:

$$z = f(u) \quad (6)$$

where  $f$  is the activation function; for example, a sigmoid function can be used. The units in Fig. 1(a) are arranged in layers, as shown in Fig. 1(b), and are used as a multilayer network. This network is called an FNN because all units in adjacent layers are connected.

#### B. Deep Convolutional Neural Network

A deep convolutional neural network (DCNN) has not only the FNN, as shown in Fig. 2(a), but also a particular layer in which only specific units between adjacent layers are combined, as shown in Fig. 2(b). These layers perform the basic image processing operations of convolution and pooling. AlexNet [28], an example of a typical DCNN, consists of five convolutional layers and three all-combining layers, with a normalization layer after the first and second convolutional layers and a maximum value pooling layer after each normalization layer and after the fifth convolutional layer.

#### C. Path Loss Prediction Using DCNN

A DCNN can obtain regression and discrimination results by repeatedly performing convolution and pooling and then inputting feature maps to a fully connected layer. In this article, the path loss is predicted by regression using input spatial data with multidimensional and location-specific environmental information, such as maps and environmental parameters related to the propagation path between transmitting and receiving points generated from these data. By extracting location-specific environmental information from spatial information data using convolution and pooling and inputting it to the FNN together with environmental parameters related to the propagation path between transmitting and receiving points, it is possible to predict path loss more accurately than conventional methods.

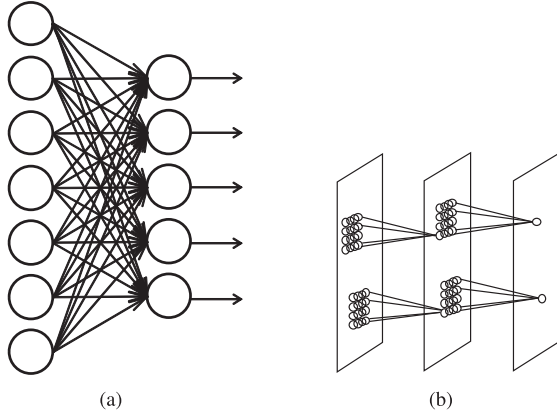


Fig. 2. Interlayer coupling in NNs. (a) Fully connected layer. (b) Convolutional layer.

### III. PROPOSED METHOD

In this section, we propose a new path loss prediction method to solve the problems of conventional methods.

#### A. Evaluation of Spatial Data Extraction Methods

We have targeted the building information in a certain range centered on the transmitting and receiving points when extracting spatial information data as features [18], [19], [20]. However, it is important to know how far from the points buildings are to extract. We have proposed a method using XGBoost [29] to predict radio propagation characteristics [30], [31]. XGBoost can output numerical values for the importance of the input features. Therefore, Nagao and Hayashi [30] visualized which regions of the map data contribute to the model's accuracy and indicated the verification results of the consistency with the mechanism of radio propagation. Nagao and Hayashi [31] also used the feature importance of map data to extract effective ranges of map data for radio propagation prediction, thereby reducing learning time without degrading prediction accuracy. In these studies, feature importance is used to extract specific ranges from map data, but how to express the environment between transmitting and receiving points as features has not been studied.

Therefore, we evaluate the regions of spatial information data that contribute to path loss prediction by visualizing the feature importance of the input spatial information data using XGBoost. There are three types of feature importance as follows. We used “gain” to select the features that contribute to improving prediction accuracy.

- 1) *Gain*: A metric of how much the objective function could be improved by adding a branch of the regression tree with a given feature.
- 2) *Weight*: The number of features used in all regression trees.
- 3) *Cover*: The average number of times a single input is branched by a feature.

We use the building occupancy rate shown in Fig. 3 as input image data. The building occupancy rate is generated by dividing a building shape polygon into a  $1 \times 1$  m mesh and calculating the area of the building included in each mesh. The

TABLE I

MAIN HYPERPARAMETERS OF XGBOOST

The number of regression trees	100
Learning rate	0.1
The maximum depth of a regression trees	8

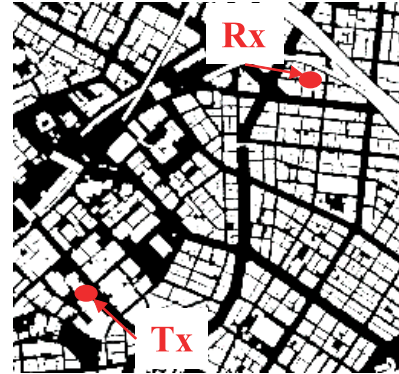


Fig. 3. Building occupancy image including transmitting and receiving points.

center of the image is the center of the transmitting and receiving points, and the image is scaled to size ( $256 \times 256$  pixels) where the transmitting and receiving points lie on the diagonal of the image, 1/4 of the way from the bottom left and top right, respectively. Table I shows the main hyperparameters used in this evaluation. In [31], it was found that increasing the maximum depth of regression trees had the most significant impact on estimation accuracy and by increasing it from 7 to 8 resulted in the convergence of estimation accuracy. Based on this result, we set the maximum depth to 8 and used default values for the other parameters. The data input to XGBoost was selected from the dataset of the urban area, which has many buildings and complex radio propagation paths, and a frequency of 2 GHz was used. Fig. 4 shows the feature importance results by training with XGBoost. As shown in Fig. 4, the three most important map areas are a rectangular area centered on the transmitting point (region 1), a rectangular area centered on the receiving point (region 2), and a specific area, including a line connecting the transmitting and receiving points (region 3). This choice can be understood from the fact that the formation of the dominant propagation path, which determines the path loss characteristics, depends on the arrangement of structures around and between the transmitting and receiving points.

As previously mentioned, using the spatial information data in three regions as the feature is suitable for path loss prediction. Therefore, Fig. 5 shows the processing flow of the proposed method for path loss prediction using three regions of spatial information data as input. First, a transmitter (Tx) image (region 1) and a receiver (Rx) image (region 2), which are rectangular images of a regular size centered on the transmitting and receiving points, respectively, are created and input to the feature extraction, which consists of convolutional and pooling layers. Next, information on the structures and terrain on the path connecting the transmitting and receiving points (region 3, hereinafter referred to as the path profile) is extracted and parameterized with a constant size regardless

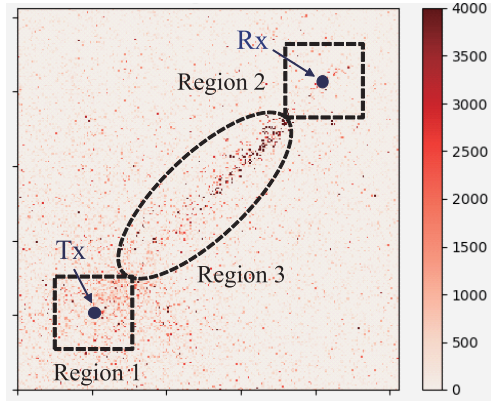


Fig. 4. Distribution of locations that contributed to improve estimation accuracy.

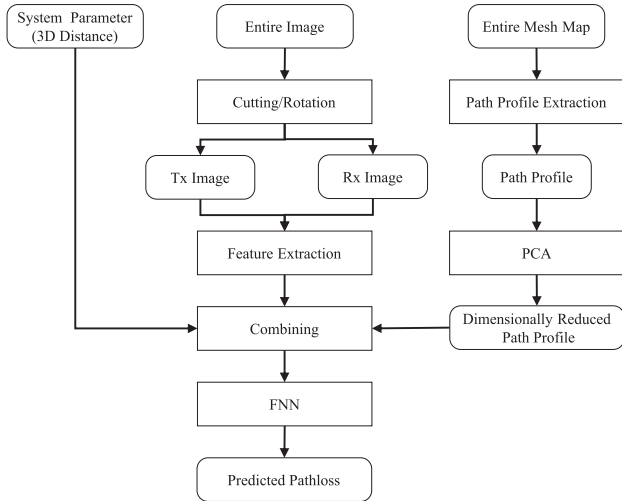


Fig. 5. Processing flow of path loss prediction proposed in this article.

of the distance using principal component analysis (PCA). Finally, the distance between the transmitting and receiving points, the features output by the feature extraction, and the environmental parameters related to the propagation path between the points are each input to the FNN to predict the path loss. In the following, we describe the image data generation method used for regions 1 and 2, the method used for region 3 to generate environmental parameters related to the propagation path between the transmitting and receiving points, and the configuration of the DCNN.

#### B. Image Data Generation Methods for Regions 1 and 2

We describe the image data used for the rectangular Tx image (region 1) and Rx image (region 2) centered on the transmitting and receiving points, respectively. In these regions, it is desirable to utilize spatial information data that contribute to path loss prediction, so the use of aerial photographs or building occupancy images generated from building polygons is considered. The details of each data point are described as follows.

1) *Aerial Photograph:* As shown in Fig. 6(a), aerial photographs [32] contain various information, such as buildings, trees, and road signs. They are considered suitable as features

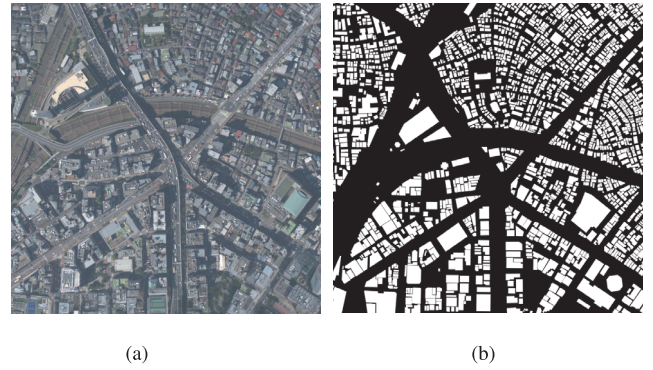


Fig. 6. Type of image data used around the transmitting and receiving points. (a) Aerial photograph data [32]. (b) Image data of building occupancy rate.

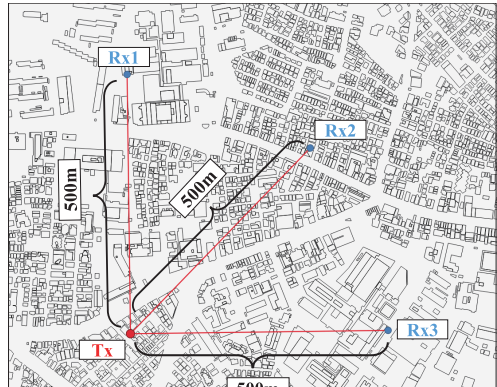
representing urban structures that affect radio propagation characteristics. Therefore, image data (grayscale image) of a rectangular area ( $256 \times 256$  pixels) centered on receiving or transmitting points are input as map data. One pixel represents an area of approximately  $1 \times 1$  m in terms of the mesh size.

2) *Building Occupancy Rate:* The building occupancy rate is generated by dividing a building shape polygon into a  $1 \times 1$  m mesh and calculating the area of the building included in each mesh. The building occupancy rate is converted into the grayscale image data. Fig. 6(b) shows the map data of building occupancy created by the aforementioned method for a rectangle ( $256 \times 256$  pixels) centered on the receiving and transmitting points. The feature of these map data is that roads are clearly represented, making it possible for the environment where radio propagation along a road becomes dominant to be extracted as a feature.

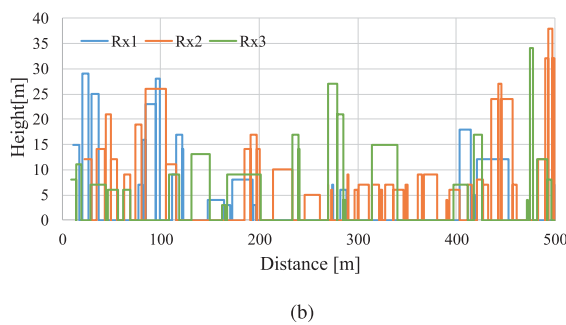
For the aerial photograph data and image data of the building occupancy rate, the image data at each receiving point were defined with the direction of the transmitting point as the coordinate axis and then rotated so that the direction of the transmitting point was to the north. This is done because the direction from the receiving point to the transmitting point has a marked effect on radio propagation. In addition, the image data at each transmitting point were determined so that the direction of the antenna was the coordinate axis and rotated so that the direction was to the north. This is because the urban structure of the surroundings centered on the orientation of the antenna is taken into consideration.

#### C. Method of Generating the Environmental Parameters Related to the Propagation Path in Region 3

As previously mentioned, we described the generation method of aerial photographs and building occupancy images applied to regions 1 and 2. The effectiveness of the path loss prediction method using these images has been clarified in our previous work [18]. Here, we describe a method for generating environmental parameters related to the propagation path between transmitting and receiving points that are applied to region 3. Path loss characteristics are determined by the dominant path, which depends on the urban structure between the transmitting and receiving points. Therefore, we consider the use of the path profile shown in Fig. 7. Even when the



(a)



(b)

Fig. 7. Example of a path profile between the transmitting and receiving points. (a) Location between the transmitting and receiving points. (b) Building distribution between the transmitting and receiving points.

distance between the transmitting and receiving points is the same, as shown in Fig. 7(a), the height distribution of structures on the path between the transmitting and receiving points takes various values, as shown in Fig. 7(b). The differences in the distribution of these path profiles are important for path loss prediction. First, we discuss the data used to generate the path profiles. As shown in Fig. 8, the building shape polygon is divided into  $25 \times 25$  m meshes, and the maximum building height within each mesh is defined as the mesh height. The building height also includes the elevation; if there are no buildings in the mesh, the elevation becomes the height of the mesh. Here, a path profile that only covers the path between the transmitting and receiving points is insufficient to capture the dominant path features generated by reflections and diffractions caused by structures and other objects between the transmitting and receiving points. Therefore, we propose a method to select paths in two ways and generate path profiles using the method shown in Fig. 9.

The method shown in Fig. 9(a) (hereinafter referred to as path profile A) is based on the idea that the contribution of structures in the propagation is scattering, including diffraction, and the height of the center of the Fresnel zone is used as a reference when scattering a single wave at all meshes in the path. As shown in Fig. 10, if the height of the  $m$ th mesh is  $H^{(m)}$ , the distances from the transmitting and receiving points to the  $m$ th mesh are  $d_t^{(m)}$  and  $d_r^{(m)}$ , respectively, and the transmitting antenna and the receiving antenna are  $h_t$  and  $h_r$ , respectively, then the height  $H_F^{(m)}$  of the center of the Fresnel



Fig. 8. Data used for path profile generation.

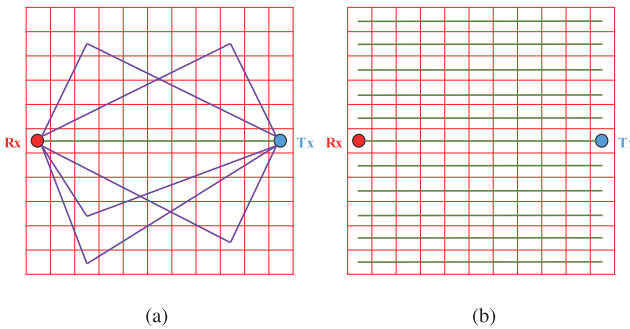


Fig. 9. Method for generating environmental parameters related to the propagation paths between the transmitting and receiving points.

zone assuming one scattering is expressed as

$$H_F^{(m)} = h_r + \frac{(h_t - h_r)d_r^{(m)}}{d_t^{(m)} + d_r^{(m)}}. \quad (7)$$

Thus, the height on each mesh based on the center of the Fresnel zone is expressed by the following equation:

$$\Delta H^{(m)} = H^{(m)} - H_F^{(m)}. \quad (8)$$

Using the height on the  $m$ th mesh calculated using (8) as an environmental parameter, a positive value of  $\Delta H^{(m)}$  can be expressed as a contribution to scattering. The region where the path profile is generated is a square with the distance between the transmitting and receiving points as one side.

Next, the method shown in Fig. 9(b) (hereinafter referred to as path profile B) parameterizes the building distribution between the transmitting and receiving points by creating a path profile on a straight line connecting the two points. Specifically, by using the values of each mesh as they are, it is possible to express the magnitude of the scattering contribution in terms of the positional relationship between the distribution of the height of structures and terrain and the path connecting the transmitting and receiving points. The region for generating the path profile is a rectangle with the distance between the transmitting and receiving points as one side and the distance specified on both sides as extended sides centered on the points. Another feature of this method is that the number of paths generated is the same regardless of the change in the distance between the points.

These methods express the scattering contribution between the transmitting and receiving points, but the length of the path

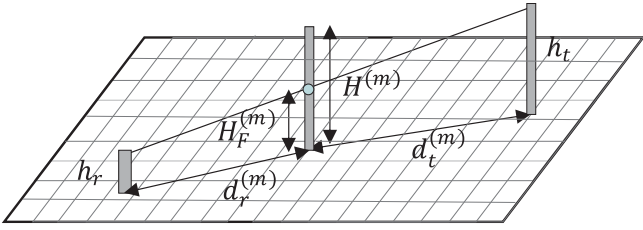


Fig. 10. Definition of height in accordance with Fresnel criteria.

profile is not uniquely determined by the distance between the transmitting and receiving points. Therefore, we consider unifying the path profile length by reducing the parameters' dimensionality through PCA. The objectives of PCA are to reduce the dimensionality of the dataset and identify new meaningful underlying variables. The key idea is to project the objects to an orthogonal subspace for their compact representations. It usually involves a mathematical procedure that transforms a number of correlated variables into a smaller number of uncorrelated variables called principal components. The  $i$ th path profile between transmitting point  $T_i$  and receiving point  $R_i$  is given by the matrix  $\mathbf{X}^{(i)}$  in the following equation:

$$\mathbf{X}^{(i)} = \begin{bmatrix} x_{11}^{(i)} & x_{12}^{(i)} & \cdots & x_{1L_i}^{(i)} \\ x_{21}^{(i)} & x_{22}^{(i)} & \cdots & x_{2L_i}^{(i)} \\ \vdots & \vdots & \ddots & \vdots \\ x_{M_i 1}^{(i)} & x_{M_i 2}^{(i)} & \cdots & x_{M_i L_i}^{(i)} \\ 0 & 0 & \cdots & 0 \\ \vdots & \vdots & \ddots & \vdots \\ 0 & 0 & \cdots & 0 \end{bmatrix} \in \mathbb{R}^{M \times L_i},$$

$$i = 1, 2, \dots, N, N+1, \dots, N+P$$

$$M = \max_i M_i \quad (9)$$

where  $M_i$ ,  $L_i$ ,  $N$ , and  $P$  represent the number of meshes, paths, training data, and test data, respectively. For path profile A, both  $L_i$  and  $M_i$  increase as the distance between the points increases. For path profile B,  $L_i$  remains constant, and  $M_i$  increases as the distance between the points increases. Therefore, when using path profile A, it is necessary to define  $L_i$  in accordance with certain criteria.

Next, we define a set of path profiles for the training data and test data as  $\mathbf{X}_{train}$  and  $\mathbf{X}_{test}$ , respectively. Let  $\mathbf{X}_{train}$  be represented by the following equation:

$$\mathbf{X}_{train} = [\mathbf{X}^{(1)}, \mathbf{X}^{(2)}, \dots, \mathbf{X}^{(N)}] \in \mathbb{R}^{M \times L}$$

$$L = \sum_{i=1}^N L_i. \quad (10)$$

Then, the PCA performs dimensionality reduction from  $M$  to  $K (< M)$ , i.e.,

$$\mathbf{Y}_{train} = [y_{k\ell}^{train}] = [\mathbf{Y}^{(1)}, \mathbf{Y}^{(2)}, \dots, \mathbf{Y}^{(N)}]$$

$$= \mathbf{W} \mathbf{X}_{train} \in \mathbb{C}^{K \times L} \quad (11)$$

$$\mathbf{Y}^{(i)} = \begin{bmatrix} y_{11}^{(i)} & y_{12}^{(i)} & \cdots & y_{1L_i}^{(i)} \\ y_{21}^{(i)} & y_{22}^{(i)} & \cdots & y_{2L_i}^{(i)} \\ \vdots & \vdots & \ddots & \vdots \\ y_{K1}^{(i)} & y_{K2}^{(i)} & \cdots & y_{KL_i}^{(i)} \end{bmatrix} \in \mathbb{R}^{K \times L_i}$$

$$i = 1, 2, \dots, N \quad (12)$$

by finding an appropriate weight matrix

$$\mathbf{W} = [w_{km}] \in \mathbb{R}^{K \times M} \quad (13)$$

such that the variance of  $y_{k\ell}^{train}$  is maximized, while the bottom zero rows in (9) are being ignored in the PCA. Note that the variances  $\text{Var}(y_{k\ell}^{train})$  satisfy the following inequality:

$$\text{Var}(y_{1\ell}^{train}) \geq \text{Var}(y_{2\ell}^{train}) \geq \cdots \geq \text{Var}(y_{K\ell}^{train}). \quad (14)$$

Here,  $y_{1\ell}^{train}, y_{2\ell}^{train}, \dots, y_{K\ell}^{train}$  are called the first, second, ..., and  $K$ th principal components, respectively. The variance and the weight  $w_{km}$  of the principal components are obtained by the eigenvalues and eigenvectors of the variance-covariance matrix of  $\mathbf{X}_{train}$ , the eigenvector corresponding to the eigenvalue  $\lambda_k$  is  $\mathbf{w}_k = [w_{k1}, w_{k2}, \dots, w_{kM}]$ , and the mean value vector is  $\boldsymbol{\mu} = [\mu_1, \mu_2, \dots, \mu_M]$ .

In path profile A, the number of paths  $L_i$  is different for each distance between the transmitting and receiving points. Hence, the matrix  $\mathbf{Y}^{(i)}$  is reduced to  $\hat{\mathbf{Y}}^{(i)}$  by extracting the first  $L_{min} = \min_i L_i$  columns, i.e.,

$$\hat{\mathbf{Y}}^{(i)} = \begin{bmatrix} y_{11}^{(i)} & y_{12}^{(i)} & \cdots & y_{1L_{min}}^{(i)} \\ y_{21}^{(i)} & y_{22}^{(i)} & \cdots & y_{2L_{min}}^{(i)} \\ \vdots & \vdots & \ddots & \vdots \\ y_{K1}^{(i)} & y_{K2}^{(i)} & \cdots & y_{KL_{min}}^{(i)} \end{bmatrix} \in \mathbb{R}^{K \times L_{min}}$$

$$i = 1, 2, \dots, N. \quad (15)$$

On the other hand, in path profile B, the number of paths  $L_i$  becomes the same for any  $i$ . Therefore, the matrix  $\hat{\mathbf{Y}}^{(i)}$  can be expressed as in (15) by defining  $L_{min} = L_i = \text{const.}$

As mentioned above,  $\hat{\mathbf{Y}}^{(i)}$  becomes the feature between the transmitting point  $T_i$  and receiving point  $R_i$ . Then, the feature  $\hat{\mathbf{Y}}_{test}$  is obtained in a similar manner to the training process, based on the PCA and by the path profile matrix  $\mathbf{X}_{test}$  and the mean value vector  $\boldsymbol{\mu}$ . The matrix  $\mathbf{X}_{test}$  is defined as

$$\mathbf{X}_{test} = [\mathbf{X}^{(N+1)}, \mathbf{X}^{(N+2)}, \dots, \mathbf{X}^{(N+P)}] \in \mathbb{R}^{M \times \tilde{L}} \quad (16)$$

$$\tilde{L} = \sum_{i=N+1}^{N+P} L_i$$

where  $\mathbf{X}_{test}$  is the deviation calculated by using the mean value  $\boldsymbol{\mu}$ . Similar to the training process, the matrix  $\mathbf{Y}_{test}$  can be calculated by the following equation:

$$\mathbf{Y}_{test} = [\mathbf{Y}^{(N+1)}, \mathbf{Y}^{(N+2)}, \dots, \mathbf{Y}^{(N+P)}]$$

$$= \mathbf{W} \mathbf{X}_{test} \in \mathbb{C}^{K \times \tilde{L}} \quad (17)$$

where the matrices  $\mathbf{Y}^{(N+1)}, \mathbf{Y}^{(N+2)}, \dots, \mathbf{Y}^{(N+P)}$  are also given by (12) for  $i = N+1, N+2, \dots, N+P$ . Finally, the new feature matrix  $\hat{\mathbf{Y}}_{test}$  can be obtained as

$$\hat{\mathbf{Y}}_{test} = [\hat{\mathbf{Y}}^{(N+1)}, \hat{\mathbf{Y}}^{(N+2)}, \dots, \hat{\mathbf{Y}}^{(N+P)}]$$

TABLE II  
LEARNING PARAMETERS

Batch size	100
Number of epochs	200
Loss function	MSE
Optimization algorithm	Adam
Activation function	ReLU
Learning rate	0.0001
Number of hidden layers	6

$$\in \mathbb{R}^{K \times PL_{min}} \quad (18)$$

where the matrices  $\hat{\mathbf{Y}}^{(N+1)}, \hat{\mathbf{Y}}^{(N+2)}, \dots, \hat{\mathbf{Y}}^{(N+P)}$  are also given by (15) for  $i = N+1, N+2, \dots, N+P$ .

As previously mentioned, the proposed method can determine the feature values of the propagation path between the transmitting and receiving points to a unique length regardless of the distance and can be used in the DCNN by making the features  $\hat{\mathbf{Y}}^{(i)}$  at the transmitting point  $T_i$  and receiving point  $R_i$  one dimension.

#### D. DCNN Model

The DCNN proposed in this article is an NN model consisting of an iterative structure of convolutional and pooling layers and fully connected layers, as shown in Fig. 11. The features of the urban structure input as an image are processed by four convolutional layers,  $C_0-C_3$ , and two pooling layers,  $P_0$  and  $P_1$ . Assuming that the size of the input of one image data is  $256 \times 256 \times 1$ , after the convolutional operation and the pooling process (max pooling) are performed with the filter size and the number of filters shown in Fig. 11(a), the data size obtained for the  $C_3$  layer is  $4056 (= 26 \times 26 \times 6)$ . As shown in Fig. 11(b), the FNN defines the hidden layer as six layers and the bias of each layer. The activation function uses the rectified linear unit (ReLU) function. Let  $q$  denote the index of the hidden layer. Then, the weight parameter  $w_q$  of each layer is given by the following equation:

$$w_q = 4096 \times \left(\frac{1}{4}\right)^{q-1}, \quad q = 1, 2, \dots, 6. \quad (19)$$

In this article, two image data points around the transmitting and receiving points are input to the feature extraction. Then, the features output by the feature extraction, environmental parameters related to the propagation path between the transmitting and receiving points, and the distance between the transmitting and receiving points are input to an FNN. Therefore, the size of the data  $S$  is expressed by the following equation:

$$S = 4056 \times 2 + L_{min} \times K + 1. \quad (20)$$

As previously mentioned, image abstraction by feature extraction generates the features that preserve the urban structure. Based on these features and environmental parameters related to the propagation path between the transmitting and receiving points, the path loss is predicted by an FNN. The learning parameters are shown in Table II.

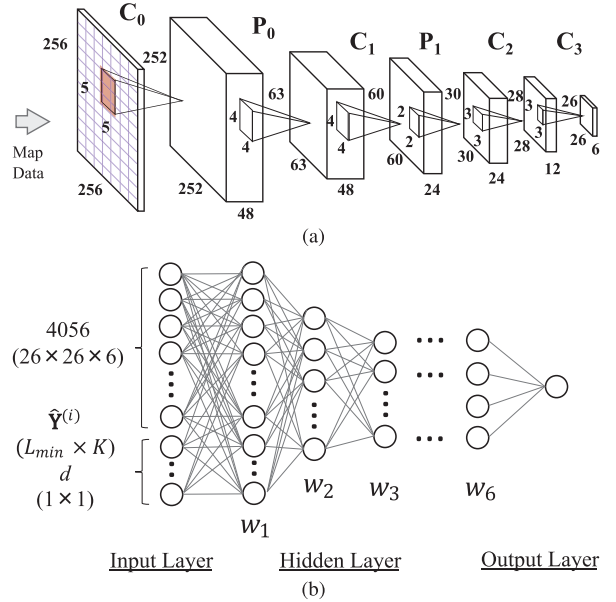


Fig. 11. DCNN model configuration. (a) Feature extraction configuration. (b) FNN configuration.

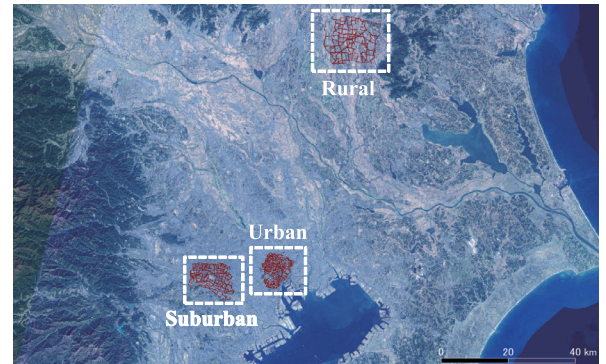


Fig. 12. Overall view of the evaluation area.

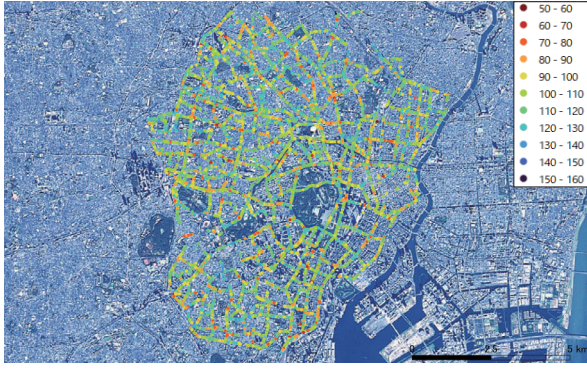
## IV. EVALUATION METHOD

We evaluated the effectiveness of the proposed model using measurement data from urban, suburban, and rural and two frequency bands (800 MHz and 2 GHz).

#### A. Dataset

Fig. 12 shows the relationship between the three areas evaluated. Urban is the central Tokyo area, suburban is an area approximately 20 km west of the center of Tokyo, and rural is an area 80 km north of the center of Tokyo. The measurement results of path loss in the urban, suburban, and rural are shown in Fig. 13.

The measurement data were obtained by installing a receiving antenna on the rooftop of a vehicle for reference signals from LTE base stations, which were already deployed in the commercial service area. The measurement data are extracted by the moving median value in a 10-m section to remove instantaneous variations. The path loss, which is the target of prediction in this study, was calculated using the following



(a)



(b)



(c)

Fig. 13. Path loss data in each area. (a) Urban. (b) Suburban. (c) Rural.

equation with the obtained RSRP:

$$PL = P_{tx} + G_{tx} - \sqrt{G_{tx}(\theta)^2 + G_{tx}(\phi)^2} - L_{tx} - RSRP \text{ [dB]} \quad (21)$$

where  $P_{tx}$  is the transmission power per reference signal of the base station,  $G_{tx}$  is the maximum gain of the transmitting antenna,  $G_{tx}(\theta)$  and  $G_{tx}(\phi)$  are the directional attenuations in the elevation and azimuth directions, respectively, and  $L_{tx}$  is the cable loss in transmission. Note that as an omnidirectional antenna was used for the Rx, the cable loss of the Rx was corrected at the time of measurement.

The dataset characteristics for each area described in Fig. 13 are shown in Table III. In urban and suburban, the data acquisition range was 100–1000 m. The base station uses a directional antenna, and the data acquired over 100 m were used because the directivity attenuation in the elevation direction increases at a short distance. In urban areas, base

TABLE III  
DATASET PARAMETERS

	Urban	Suburban	Rural
Frequency		800 MHz / 2 GHz	
Measurement method		Car	
Height of Rx		1.7 m	
Total number of data points	50000	50000	50000
Number of test data	5000	5000	5000
Distance between Tx and Rx	100 to 1000 m	100 to 1000 m	100 to 2500 m

station density is high, and at long distances, signal separation becomes difficult due to the overlap of base station-specific signal physical cell IDs (PCIs), so we used data less than 1000 m away. In rural areas, the maximum distance is set to 2500 m because the coverage of one base station is wide, and the base station density is sparse. The spatial information data to be input to the proposed model are aerial photographs or building occupancy image data generated by the method described in Section III-B for regions 1 and 2. In region 3, we used the environmental parameters  $\mathbf{Y}_{train}$  and  $\mathbf{Y}_{test}$ , which are the environmental parameters related to the propagation paths between the transmitting and receiving points generated by path profiles A and B using the method described in Section III-C. Since the minimum distance between the transmitting and receiving points is 100 m, the minimum number of meshes  $M_i$  to be calculated is 5 for a mesh size of 25 m. Since the number of meshes  $M_i$  to be calculated increases as the distance between the transmitting and receiving points increases, it is necessary to define the number of principal components to be used, that is, the value of  $K$ . In this study, the value of  $K$  is set to the minimum number of meshes, 5. The number of paths  $L_i$  increases as the distance between the transmitting and receiving points increases when path profile A is used. Therefore, the number of paths  $L_{min}$  generated by the path profile is 21 for a distance of 100 m between the transmitting and receiving points, so the value of  $L_{min}$  is set to 21 for path profile A. In path profile B, the number of paths  $L_i$  is determined by the length vertical to the line connecting the transmitting and receiving points. By defining this length to be equivalent to the input data image size of 256 m per side, considering the mesh size of 25 m, the number of paths  $L_{min}$  is constant 11, consisting of one line connecting the transmitting and receiving points, plus five lines above and below. Therefore, in path profile B, the number of paths  $L_{min}$  is constant 11, regardless of the distance between the transmitting and receiving. Thus, the dimensions of each path profile are  $(L_{min}, K) = (21, 5)$  for path profile A and  $(L_{min}, K) = (11, 5)$  for path profile B. Therefore, the data size to be input to the FNN is 8218 and 8168 for path profiles A and B, respectively, based on (20).

#### B. Evaluation Method

As shown in Table III, the total number of data points in each area is 50 000, 10% of which is test data (5000 points) and the remainder is training data (45 000 points), and k-fold cross validation is performed. The estimation accuracy

is evaluated using root-mean-square error (RMSE), mean absolute percentage error (MAPE), and the Pearson correlation coefficient (PCC), where  $N$  is the number of data points,  $\{r_1, \dots, r_N\}$  are the measured values, and  $\{z_1, \dots, z_N\}$  are the predicted values. The RMSE, MAPE, and PCC are given by

$$\text{RMSE} = \sqrt{\frac{1}{N} \sum_{i=1}^N (r_i - z_i)^2} \quad (22)$$

$$\text{MAPE} = \frac{100}{N} \sum_{i=1}^N \left| \frac{r_i - z_i}{r_i} \right| \quad (23)$$

$$\text{PCC} = \frac{\text{cov}(r, z)}{\sigma_r \sigma_z} \quad (24)$$

where  $\text{cov}(r, z)$  is the covariance of  $r$  and  $z$ , and  $\sigma_r$  and  $\sigma_z$  are the standard deviations of  $r$  and  $z$ , respectively. The final evaluation is performed using the average of ten results for each of the three measures of accuracy calculated by  $k$ -fold cross validation. This avoids an evaluation that depends on specific test data.

## V. EVALUATION RESULTS

In this section, we describe the evaluation result of the proposed method. First, we examine the proposed method's effectiveness for different image data and path profiles A and B for a frequency of 2 GHz in urban areas. Then, we compare the estimation accuracy of the proposed method for urban, suburban, and rural. Next, we compare the estimation accuracy for each frequency. Finally, we examine the configuration of the proposed DCNN model and its estimation accuracy.

### A. Evaluation Results in Urban

Fig. 14 and Table IV show the evaluation results when aerial photographs or building occupancy images and numerical data of path profile A or B as environmental parameters related to the propagation path between the transmitting and receiving points are applied to the input data to the DCNN model. For comparison, we include the results of a method that uses aerial photographs and building occupancy images only [18] and a method that uses the area between the transmitting and receiving points as a single image [22], which the previous study has proposed. The evaluation results for each method show that the estimation accuracy is higher when building occupancy images are used as input data. By using the building occupancy image, the proposed model can clearly distinguish the buildings from the road. In other words, the two following features of the propagation characteristics are captured. One feature is the direct waves that are dominant in the LOS region and reflections along the road in the LOS region. The other is route propagation along roads, which is dominant in the NLOS region and routes arriving from over the buildings. Next, in the comparison of path profiles A and B, it can be seen that the estimation accuracy for path profile A did not improve compared with the conventional method [18], [22], while that for path profile B improved. The combination of path profile B and the building occupancy image has the highest estimation accuracy with an RMSE of 4.27 dB, an MAPE of 2.22%, and a PCC of 0.96. It is considered that the

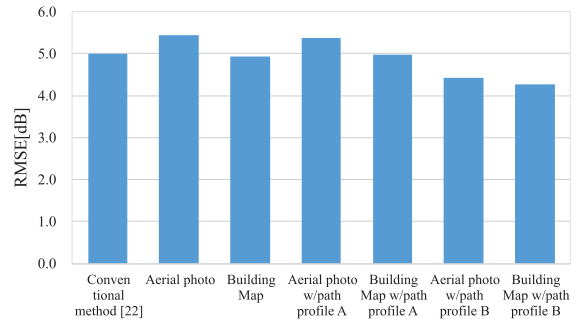


Fig. 14. RMSE comparison of input data types and the proposed method.

TABLE IV  
RMSE, MAPE, AND PCC COMPARISON OF INPUT DATA TYPES AND THE PROPOSED METHOD

	RMSE	MAPE	PCC
Conventional method [22]	4.99	3.01	0.90
Aerial photo	5.44	2.90	0.93
Building map	4.94	2.58	0.94
Aerial photo w/ path profile A	5.37	2.91	0.93
Building map w/ path profile A	4.97	2.66	0.94
Aerial photo w/ path profile B	4.43	2.35	0.95
Building map w/ path profile B	<b>4.27</b>	<b>2.22</b>	<b>0.96</b>

dominant propagation paths that contribute to the propagation loss are captured as features by using propagation environment parameters between the transmitting and receiving points as features, which have not been considered in conventional methods. Although the conventional method [18] represents the area between the transmitting and receiving points as a single image, the image size is scaled in accordance with the distance, and this may be the reason that the estimation accuracy did not improve due to the different effects on propagation characteristics caused by surrounding buildings, even if the propagation path was the same. In addition, with the conventional method, as the distance between the transmitting and receiving points increases, the information between them is lost, and the estimation accuracy may deteriorate. Therefore, we calculated the RMSE for every 100 m and compared the distance characteristics between the proposed and conventional methods, as shown in Fig. 15. In this figure, the proposed method can suppress the degradation of estimation accuracy at all distances compared with the conventional method. The proposed method can consider environmental parameters related to the propagation path between the transmitting and receiving points even when the distance between the points increases, which presumably contributes to the improvement in estimation accuracy.

Next, we discuss the reason that the estimation accuracy does not improve in path profile A. For path profile A, the number of path profiles  $\ell$  increases because the size of the square region containing the transmitting and receiving points becomes larger with the increasing distance between the points. In this method, to unify the dimension of the features  $\hat{\mathbf{Y}}^{(i)}$  input to the DCNN model, the number of path profiles is set to  $L_{\min} = 21$ , which is determined by the minimum distance between the transmitting and receiving points, and the path profiles are selected from those with short distances,

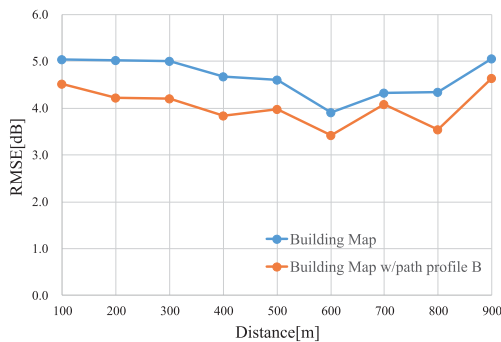


Fig. 15. Relationship between distance and estimation accuracy.

that is, those with small path loss. It is possible to improve the estimation accuracy by optimizing the selection method of the path profile. However, selecting the path profile requires a reference to other parameter information, such as diffraction angle, which contributes to the path loss characteristics and is related to the cost of parameter generation. Therefore, considering the cost of parameter generation, it is assumed that path profile B is effective. Next, we evaluate the relationship between the number of parameters to be added and the estimation accuracy when using the proposed path profile method. As an evaluation index, we use the contribution ratio, which is the ratio of the increase in the number of parameters to the improvement in RMSE. The contribution ratio is given by

$$\text{Contribution rate} = \frac{\text{RMSE}_{pro} - \text{RMSE}_{con}}{\text{NumPa}_{pro} - \text{NumPa}_{con}} \quad (25)$$

where  $\text{RMSE}_{pro}$  and  $\text{RMSE}_{con}$  and  $\text{NumPa}_{pro}$  and  $\text{NumPa}_{con}$  are the RMSE and number of parameters of the proposed and conventional methods, respectively. Fig. 16 shows the relationship between the estimation accuracy and contribution ratio when using aerial photographs and building occupancy images. Fig. 16 also shows that the contribution ratio of path profile B is higher than that of path profile A for both images. As previously mentioned, this is because, with path profile A, the added parameters do not necessarily contribute to the path loss characteristics between the transmitting and receiving points, and selecting the path profile is necessary. Comparing the aerial photograph and building occupancy image, it can be seen that the contribution is  $-1.8\%$  for the aerial photograph and  $-1.2\%$  for the building occupancy, with the aerial photograph being larger. It is considered that the addition of the path profile enables propagation path information to be represented, which could not be represented only by the aerial photograph. Next, since the highest estimation accuracy is achieved when building occupancy images and path profile B are used, the distance characteristics of the path loss estimates are compared with the measured data and existing statistical models. The statistical model used for comparison is the Urban Micro (UMi) model [24], which is specified for urban microcell environments. The UMi model is divided into the LOS and NLOS models, and the UMi NLOS model was used in the environment where the measurement data were acquired because there are only a few locations with the LOS from the

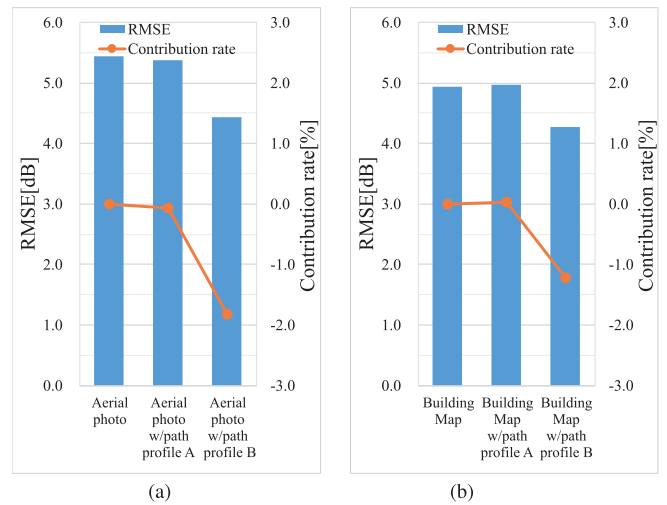


Fig. 16. Relationship between the estimation accuracy and the contribution ratio. (a) Aerial photograph. (b) Building occupancy image.

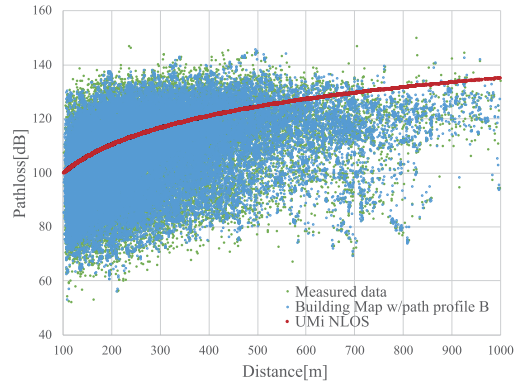


Fig. 17. Comparison of path loss and distance characteristics.

base station. Fig. 17 shows the results of comparing path loss and distance characteristics, where the statistical model is a site-generic model and cannot estimate even the shadowing, as shown in the measured data. However, the proposed method using path Profile B can estimate the path loss at each location by treating the propagation environment around and between the transmitting and receiving points as a feature. The same results were obtained when comparing path profiles A and B with the conventional method on data other than urban. Therefore, the following discusses the evaluation results for each geographical feature and frequency when path profile B is used.

### B. Evaluation Results in Each Area

The evaluation results for urban, suburban, and rural when using path profile B are shown in Fig. 18. The results show that the inclusion of path profile B is more effective than the conventional method in all three areas. In urban and suburban, the combination of the building occupancy image and path profile B has the highest estimation accuracy. However, it can be seen that the estimation accuracy is the highest in rural when combining the aerial photograph image and path profile B. Unlike urban and suburban, rural has a low building density.

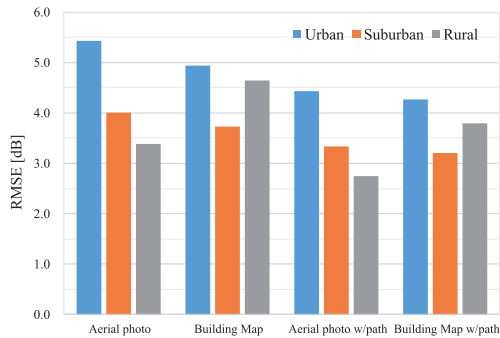


Fig. 18. Comparison of estimation accuracy in urban, suburban, and rural when using path profile B.

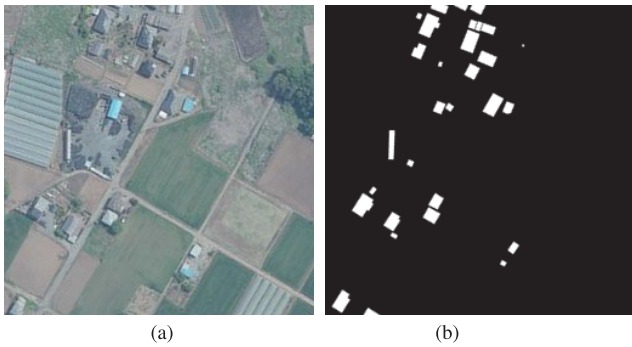


Fig. 19. Input image in rural. (a) Aerial photograph. (b) Building occupancy image.

Comparing the aerial photograph and the building occupancy image at a specific location, as shown in Fig. 19, it is possible that all objects except buildings are recognized as roads in the building occupancy image. However, with aerial photographs, it is possible to consider information other than buildings, such as trees. Therefore, it is considered that the increase in path loss due to shadowing other than buildings, such as trees, which is unique to rural, can be captured as a feature. Comparing the estimation accuracy of urban, suburban, and rural, an RMSE of 2.74 dB is the most accurate for rural, followed by RMSEs of 3.20 and 4.27 dB for suburban and urban, respectively. The aforementioned results are reasonable because the more urban the area is, the greater the scattering effect due to the increase in structures, and the more complex the propagation environment becomes.

### C. Evaluation Result for Each Frequency

In this section, we present the estimation accuracy results for different frequency bands in urban, suburban, and rural. Fig. 20 shows the results for urban, suburban, and rural, where the estimation accuracy is higher at 800 MHz than at 2 GHz in each area. The highest estimation accuracy in urban and suburban is achieved by the combination of the building occupancy image and path profile B, and the difference in estimation accuracy is approximately 0.65 dB. In rural, the difference in estimation accuracy between the combination of aerial photographs and path profile B, which has the highest estimation accuracy, is approximately 0.19 dB, which

is approximately the same. The reasons for the difference in estimation accuracy between urban and suburban are discussed in the following. The proposed method extracts the features related to the dominant propagation paths that contribute to the path loss from image data in three regions: around the transmitting point, receiving point, and along the transmitting and receiving path. Since the Fresnel zone is smaller at higher frequencies, it is expected that most of the Fresnel zone is intercepted when shadowing occurs on the dominant propagation path, resulting in greater shadowing loss. Since the proposed method generates image data based on building shape polygons, it is difficult to reproduce structures that shadow the Fresnel zone as in a real environment. Therefore, the estimation accuracy is considered to deteriorate as the frequency increases. Since rural has a high LOS ratio and the propagation path is close to the LOS, there is no difference in estimation accuracy because it is not affected by the aforementioned effects.

### D. Computational Complexity and Estimation Accuracy of the Proposed Model

In this section, we evaluate the configuration of the proposed model in terms of estimation accuracy and computational complexity. In NNs, as the number of layers and neurons increases, the expressiveness of the results improves, but the computational complexity increases. Therefore, selecting layers and the number of neurons is necessary, considering the amount of computational complexity and estimation accuracy. When using image data recognition, as in the proposed method, it is fundamental to set up many neurons in the first layer and gradually reduce the number of neurons, so the number of neurons for layers is determined using (19). However, there is a tradeoff between the estimation accuracy and the amount of computational complexity for the number of layers, and it is necessary to clarify the number of layers considering both. Therefore, we evaluated the estimation accuracy and the computational complexity in the 2-GHz band in urban areas when using image data of the building occupancy image and path profile B, which provide the highest estimation accuracy. The computational complexity is defined by floating-point operations (FLOPs), which are the sum of the multiplications of the DCNN model. Assuming the input feature map size  $D_F \times D_F \times CH_1$ , the output feature map size  $D_F \times D_F \times CH_2$ , and the kernel size  $D_k \times D_k$  for a single convolutional layer in the feature extraction section, the computational complexity  $Cal_{cov}$  is represented by the following equation:

$$Cal_{cov} = D_k^2 C H_1 C H_2 D_F^2. \quad (26)$$

If the number of input data is  $N_{in}$  and the number of output data is  $N_{out}$  in one layer of the FNN, the computational complexity  $Cal_{FNN}$  is represented by the following equation:

$$Cal_{FNN} = N_{in} N_{out}. \quad (27)$$

As mentioned above, the computational complexity  $Cal_{DCNN}$  of the DCNN model with one convolutional layer and one FNN can be calculated by the following equation:

$$Cal_{DCNN} = Cal_{cov} + Cal_{FNN}. \quad (28)$$

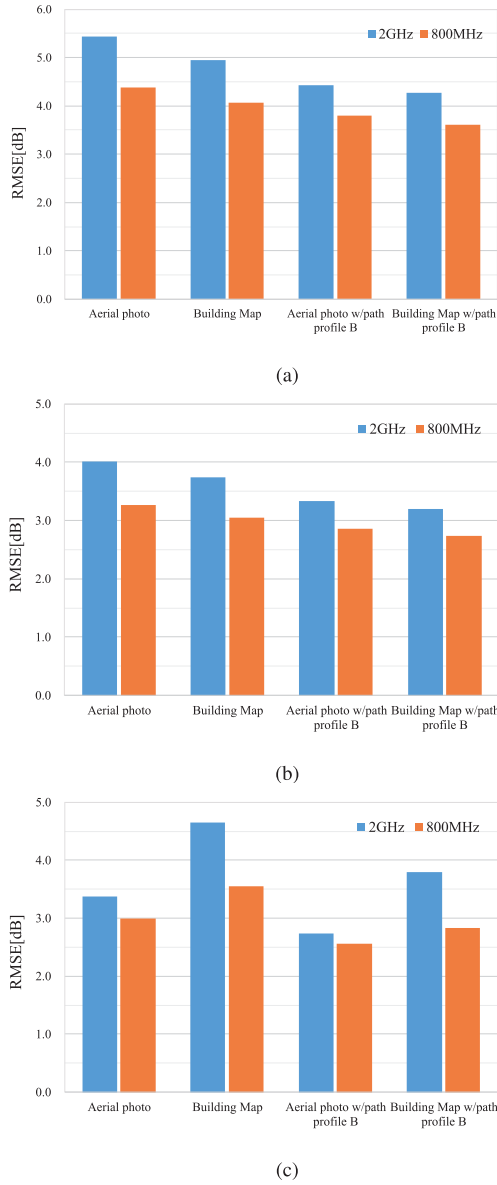


Fig. 20. RMSE comparison between 800 MHz and 2 GHz in each area.  
(a) Urban. (b) Suburban. (c) Rural.

Therefore, the computational complexity of the DCNN model can be calculated by (28), depending on the number of convolutional and FNN layers.

Fig. 21 shows the results of the estimation accuracy and computational complexity for different numbers of FNN layers. The computational complexity is shown in FLOPs. Fig. 21 also shows that the RMSE improves as the number of layers increases along with the computational complexity. In particular, when the number of layers is increased from six to seven, the number of neurons in the middle layer increases, significantly increasing computational complexity. In addition, when the number of layers is increased to eight or more, the computation becomes difficult under the conditions shown in Table II due to hardware constraints. Based on these results, the number of layers was set to six from the perspective of the amount of improvement in estimation accuracy and

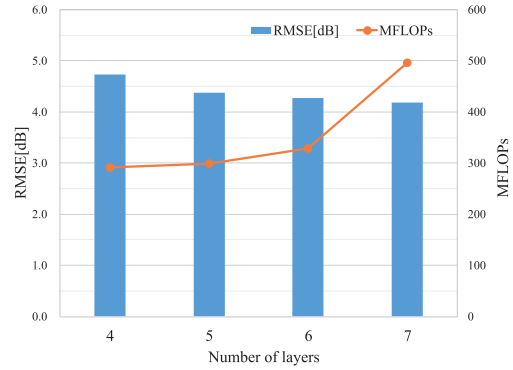


Fig. 21. Estimation accuracy and computational complexity for different numbers of FNN layers.

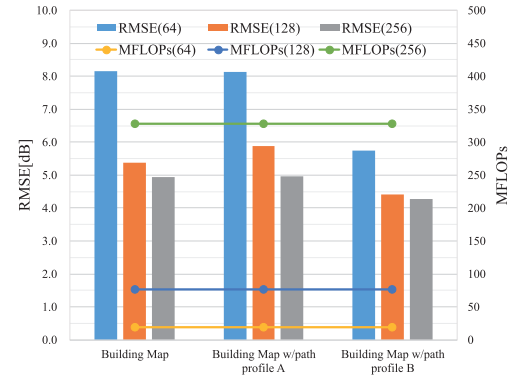


Fig. 22. Estimation accuracy and computational complexity for different image sizes.

computational complexity. Next, we evaluate the relationship between the estimation accuracy and computational complexity for the image size input to the DCNN model using data at 2 GHz in urban areas. Fig. 22 shows the results when the path profiles are combined with building occupancy images that provide high estimation accuracy, using three input image sizes of  $64 \times 64$ ,  $128 \times 128$ , and  $256 \times 256$  pixels. This figure shows that when the input image size is  $64 \times 64$  pixels, the propagation environment around the transmitting and receiving points cannot be fully captured, and the estimation accuracy deteriorates. When the input image size is increased to  $256 \times 256$  pixels, the computational complexity increases by 17, but the estimation accuracy improves up to 3.22 dB. An image size of  $256 \times 256$  pixels is considered appropriate to adequately capture the propagation environment around the transmitting and receiving points and to obtain high estimation accuracy. On the other hand, expanding the image size to  $512 \times 512$  pixels is unrealistic because it is difficult to calculate under the conditions shown in Table II due to hardware limitations. From the aforementioned results, the proposed DCNN model in this article uses the configuration shown in Fig. 5. The increase in computational complexity is less than 1% for the proposed method compared with the conventional method, indicating that the proposed method is a model that reduces the increase in computational complexity and improves the estimation accuracy.

## VI. CONCLUSION

In this article, we proposed a method to parameterize the environment on the propagation path in the region between the transmitting and receiving points with a constant size regardless of the distance and use it together with the images around the transmitting and receiving points. In this method, the dominant path that contributes to the propagation loss characteristics depends on the urban structure between the transmitting and receiving points, and the estimation accuracy is improved by parameterizing the environment on the propagation path. We clarified the effectiveness of the proposed method using 800-MHz and 2-GHz band measured data obtained over a wide area of  $500 \text{ km}^2$  covering urban, suburban, and rural areas. From the evaluation results, we found that the estimation accuracy is higher when path profile B, which represents the building distribution, is used rather than path profile A, which represents the scattering distribution.

In the urban and suburban areas, the combination of path profile B and the building occupancy image has the highest estimation accuracy, while in the rural area, the combination of path profile B and the aerial photograph has the highest estimation accuracy. In the urban and suburban areas, the high density of buildings enables to clearly distinguish between buildings and roads by using building occupancy images, which are thought to capture the environment that forms the dominant propagation path as a feature. However, in the rural area with low building density, information other than buildings, such as trees, which affect propagation loss characteristics, is needed, so the use of aerial photographs is effective. Comparing the estimation accuracy for each frequency, the estimation accuracy is higher at 800 MHz than at 2 GHz. This is because the Fresnel zone is smaller at higher frequencies, and structures must be simulated more precisely.

Future tasks include diversifying the features used as input data and improving estimation accuracy when the amount of measured data used for training is small. In the former, in addition to extracting shields using aerial photographs and building occupancy images, the use of point clouds and other data should improve the accuracy by developing modeling that considers precise structures such as street trees, which is an issue in millimeter waves. In the latter, when only a small amount of the measured data is available such as introducing a new frequency, a highly accurate model can be pretrained using a large amount of the measured data in the frequency band in operation, and then, the model is transferred to a new frequency model by transfer learning, which should be more efficient.

## REFERENCES

- [1] T. K. Sarkar, Z. Ji, K. Kim, A. Medouri, and M. Salazar-Palma, "A survey of various propagation models for mobile communication," *IEEE Antennas Propag. Mag.*, vol. 45, no. 3, pp. 51–82, Jun. 2003.
- [2] Y. Wang, S. Safavi-Naeini, and S. K. Chaudhuri, "A hybrid technique based on combining ray tracing and FDTD methods for site-specific modeling of indoor radio wave propagation," *IEEE Trans. Antennas Propag.*, vol. 48, no. 5, pp. 743–754, May 2000.
- [3] R. Valenzuela, "A ray tracing approach to predicting indoor wireless transmission," in *Proc. IEEE 43rd Veh. Technol. Conf.*, Apr. 1993, pp. 214–218.
- [4] S.-C. Kim et al., "Radio propagation measurements and prediction using three-dimensional ray tracing in urban environments at 908 MHz and 1.9 GHz," *IEEE Trans. Veh. Technol.*, vol. 48, no. 3, pp. 931–946, May 1999.
- [5] Z. Yun and M. F. Iskander, "Ray tracing for radio propagation modeling: Principles and applications," *IEEE Access*, vol. 3, pp. 1089–1100, 2015.
- [6] M. Hata, "Empirical formula for propagation loss in land mobile radio services," *IEEE Trans. Veh. Technol.*, vol. VT-29, no. 3, pp. 317–325, Aug. 1980.
- [7] F. Ikegami, S. Yoshida, T. Takeuchi, and M. Umebara, "Propagation factors controlling mean field strength on urban streets," *IEEE Trans. Antennas Propag.*, vol. AP-32, no. 8, pp. 822–829, Aug. 1984.
- [8] J. Walfisch and H. L. Bertoni, "A theoretical model of UHF propagation in urban environments," *IEEE Trans. Antennas Propag.*, vol. AP-36, no. 12, pp. 1788–1796, Dec. 1988.
- [9] E. Ostlin, H. Zepernick, and H. Suzuki, "Macrocell path-loss prediction using artificial neural networks," *IEEE Trans. Veh. Technol.*, vol. 59, no. 6, pp. 2735–2747, Jul. 2010.
- [10] M. Ayadi, A. Ben Zineb, and S. Tabbane, "A UHF path loss model using learning machine for heterogeneous networks," *IEEE Trans. Antennas Propag.*, vol. 65, no. 7, pp. 3675–3683, Jul. 2017.
- [11] U. Masood, H. Farooq, and A. Imran, "A machine learning based 3D propagation model for intelligent future cellular networks," in *Proc. IEEE Global Commun. Conf. (GLOBECOM)*, Dec. 2019, pp. 1–6.
- [12] J. Thrane, M. Artuso, D. Zibar, and H. L. Christiansen, "Drive test minimization using deep learning with Bayesian approximation," in *Proc. IEEE 88th Veh. Technol. Conf.*, Aug. 2018, pp. 1–5.
- [13] J. Thrane, D. Zibar, and H. L. Christiansen, "Model-aided deep learning method for path loss prediction in mobile communication systems at 2.6 GHz," *IEEE Access*, vol. 8, pp. 7925–7936, 2020.
- [14] T. Imai, K. Kitao, and M. Inomata, "Radio propagation prediction model using convolutional neural networks by deep learning," in *Proc. 13th Eur. Conf. Antennas Propag. (EuCAP)*, Mar. 2019, pp. 1–5.
- [15] J. Thrane, B. Sliwa, C. Wietfeld, and H. L. Christiansen, "Deep learning-based signal strength prediction using geographical images and expert knowledge," in *Proc. IEEE Global Commun. Conf.*, Dec. 2020, pp. 1–6.
- [16] N. Kuno, W. Yamada, M. Inomata, M. Sasaki, Y. Asai, and Y. Takatori, "Evaluation of characteristics for NN and CNN in path loss prediction," in *Proc. Int. Symp. Antennas Propag. (ISAP)*, Jan. 2021, pp. 61–62.
- [17] S. P. Sotirovdis, P. Sarigiannidis, S. K. Goudos, and K. Siakavara, "Fusing diverse input modalities for path loss prediction: A deep learning approach," *IEEE Access*, vol. 9, pp. 30441–30451, 2021.
- [18] T. Hayashi, T. Nagao, and S. Ito, "A study on the variety and size of input data for radio propagation prediction using a deep neural network," in *Proc. 14th Eur. Conf. Antennas Propag. (EuCAP)*, Mar. 2020, pp. 1–5.
- [19] K. Inoue, K. Ichige, T. Nagao, and T. Hayashi, "Radio propagation prediction using deep neural network and building occupancy estimation," *IEICE Commun. Exp.*, vol. 9, no. 10, pp. 506–511, Oct. 2020.
- [20] K. Inoue, K. Ichige, T. Nagao, and T. Hayashi, "Radio propagation prediction using neural network and building occupancy estimation," in *Proc. Int. Symp. Antennas Propag. (ISAP)*, Jan. 2021, pp. 315–316.
- [21] K. Inoue, K. Ichige, T. Nagao, and T. Hayashi, "On the building map for radio propagation prediction using machine learning," in *Proc. IEEE 32nd Annu. Int. Symp. Pers., Indoor Mobile Radio Commun. (PIMRC)*, Sep. 2021, pp. 842–847.
- [22] K. Inoue, K. Ichige, T. Nagao, and T. Hayashi, "Learning-based prediction method for radio wave propagation using images of building maps," *IEEE Antennas Wireless Propag. Lett.*, vol. 21, no. 1, pp. 124–128, Jan. 2022.
- [23] P. Kyosti et al., "WINNER II channel models," Eur. Commission, Brussels, Belgium, IST-WINNER, Tech. Rep., D1.1.2, 2009.
- [24] *Study on Channel Model for Frequencies From 0.5 to 100 GHz*, 3GPP, document TR 38.901, Dec. 2019.
- [25] H. H. Xia, "A simplified analytical model for predicting path loss in urban and suburban environments," *IEEE Trans. Veh. Technol.*, vol. 46, no. 4, pp. 1040–1046, Nov. 1997.
- [26] *Propagation Data and Prediction Methods for the Planning of Short-Range Outdoor Radiocommunication Systems and Radio Local Area Networks in the Frequency Range 300 MHz to 100 GHz*, document ITU-R P.1411-7, P Series, ITU, Geneva, 2013.
- [27] M. Leshno, V. Y. Lin, A. Pinkus, and S. Schocken, "Multilayer feedforward networks with a nonpolynomial activation function can approximate any function," *Neural Netw.*, vol. 6, no. 6, pp. 861–867, Jan. 1993.

- [28] A. Krizhevsky, I. Sutskever, and G. E. Hinton, "ImageNet classification with deep convolutional neural networks," in *Proc. Adv. Neural Inf. Process. Syst.*, vol. 25, Dec. 2012.
- [29] T. Chen and C. Guestrin, "XGBoost: A scalable tree boosting system," in *Proc. 22nd ACM SIGKDD Int. Conf. Knowl. Discovery Data Mining*, Aug. 2016, pp. 785–794.
- [30] T. Nagao and T. Hayashi, "Study on radio propagation prediction by machine learning using urban structure maps," in *Proc. 14th Eur. Conf. Antennas Propag. (EuCAP)*, Mar. 2020, pp. 1–5.
- [31] T. Nagao and T. Hayashi, "A study on urban structure map extraction for radio propagation prediction using XGBoost," in *Proc. 15th Eur. Conf. Antennas Propag. (EuCAP)*, Mar. 2021, pp. 1–5.
- [32] Seamlessphoto. *Geospatial Information Authority of Japan*. Accessed: Oct. 1, 2022. [Online]. Available: <https://maps.gsi.go.jp/development/ichiran.html>



**Takahiro Hayashi** received B.E. and M.E. degrees in information and communication engineering from Yokohama National University, Yokohama, Japan, in 2002 and 2004, respectively.

In 2004, he joined KDDI Corporation, Fujimino, Japan, where he was engaged in telecommunication network planning and optimization. Since 2010, he has been engaged in the research and development of mobile communication systems with KDDI Research, Inc, Fujimino. He is currently involved in the development of new frequency bands and radio propagation prediction by using machine learning.

Mr. Hayashi received the Young Researcher's Award from IEICE in 2011.



**Koichi Ichige** (Member, IEEE) received B.E., M.E., and Dr.Eng. degrees in electronics and computer engineering from the University of Tsukuba, Tsukuba, Japan in 1994, 1996, and 1999, respectively.

He became a Research Associate at the Department of Electrical and Computer Engineering, Yokohama National University, Yokohama, Japan, in 1999, where he is currently a Professor. He was a Visiting Researcher at the Swiss Federal Institute of Technology Lausanne (EPFL), Lausanne, Switzerland, from 2001 to 2002. His research interests include digital signal processing, approximation theory, and their applications to image processing and mobile communication.

Dr. Ichige serves as a Vice-Chair for the Signal Processing Technical Committee of IEICE, Japan. He served as an Associate Editor for IEEE TRANSACTIONS ON INDUSTRIAL ELECTRONICS from 2004 to 2008 and Journal of Circuits, Systems and Computers (JCSC) from 2012 to 2014. He also served as an Associate Editor for IEICE Transactions on Fundamentals of Electronics, Communications and Computer Sciences (IEICE-EA) from 2015 to 2018, where he served as an Editor from 2019 to 2021.